Journal of
Manufacturing and Materials Processing

MDPI

Article

Microstructure and Mechanical Properties of Al6060/TiB_2 Aluminum Matrix Composites Produced via Ultrasonically Assisted Stir Casting and Radial-Shear Rolling

Maxat Abishkenov [1,*], Ilgar Tavshanov [1], Nikita Lutchenko [2], Kairosh Nogayev [1], Zhassulan Ashkeyev [1] and Siman Kulidan [1]

[1] Department of Technological Machines and Transportation, Karaganda Industrial University, Temirtau 101400, Kazakhstan; i.tavshanov@tttu.edu.kz (I.T.); k.nogayev@tttu.edu.kz (K.N.); zh.ashkeyev@tttu.edu.kz (Z.A.); s.kulidan@tttu.edu.kz (S.K.)
[2] Core Facilities—Office the Provost, Nazarbayev University, Astana 010000, Kazakhstan; nikita.lutchenko@nu.edu.kz
* Correspondence: m.abishkenov@tttu.edu.kz

Abstract

Lightweight aluminum matrix composites with superior strength and structural integrity are in high demand for next-generation transportation and aerospace applications. In this work, Al6060-based composites reinforced with ≈2 wt.% TiB_2 were produced using a hybrid processing route that combines ultrasonically assisted stir casting with radial-shear rolling (RSR). This strategy enabled uniform particle dispersion, strong matrix–reinforcement bonding, and substantial microstructural refinement (grain size 4–6 μm) with reduced porosity. Consequently, the Al6060/TiB_2 composites demonstrated substantial gains over the as-cast alloy, combining a yield strength of 108.6 MPa, ultimate tensile strength of 156.9 MPa, and microhardness of 76.3 HV0.2 with a balanced ductility of ~9%. The demonstrated synergy of ultrasound-assisted casting and severe plastic deformation highlights a scalable pathway for fabricating high-performance aluminum composites, positioning them as promising candidates for aerospace, automotive, and other advanced engineering sectors.

Keywords: Al6060 alloy; aluminum matrix composites (AMCs); TiB_2 reinforcement; ultrasonically assisted stir casting; radial shear rolling (RSR); microstructure evolution; mechanical properties

Academic Editor: Luis Filipe Menezes

Received: 27 August 2025
Revised: 6 September 2025
Accepted: 7 September 2025
Published: 9 September 2025

Citation: Abishkenov, M.; Tavshanov, I.; Lutchenko, N.; Nogayev, K.; Ashkeyev, Z.; Kulidan, S. Microstructure and Mechanical Properties of Al6060/TiB_2 Aluminum Matrix Composites Produced via Ultrasonically Assisted Stir Casting and Radial-Shear Rolling. *J. Manuf. Mater. Process.* **2025**, *9*, 309. https://doi.org/10.3390/jmmp9090309

1. Introduction

The current progress in materials science and mechanical engineering is strongly influenced by the growing demand for materials that combine low density, high strength, and resistance to extreme service conditions. In this regard, metal matrix composites (MMCs) have attracted considerable attention. These materials consist of a metallic or alloy matrix reinforced with either a single type of ceramic particle (binary composite) or multiple types (hybrid composite), thus integrating the advantages of both classes of materials [1,2]. According to Straits Research [3], the global MMC market is valued at USD 547.34 billion in 2024 and is projected to reach USD 1269.64 billion by 2033, with a compound annual growth rate of 9.8%. Within this segment, aluminum matrix composites (AMCs) dominate in both market share and growth rate, owing to the low density of aluminum combined with its corrosion resistance, thermal and electrical conductivity, and

the substantial improvement of mechanical performance provided by reinforcement [4,5]. Key application areas driving this expansion include the aerospace [6], automotive [7], marine [8], and defense [9] industries, where the demand for weight reduction and high-performance materials is becoming increasingly critical.

The industrial fabrication routes for aluminum matrix composites (AMCs) are generally categorized into three groups: (i) solid-state processes, (ii) liquid-state processes, and (iii) deposition processes, as comprehensively reviewed in [10]. Among these, stir casting remains one of the most attractive liquid-state techniques due to its versatility, low equipment cost, scalability, and ability to achieve a reasonably uniform distribution of the reinforcing phase [11–14]. In the past decade, increasing attention has been paid to two-step processing strategies that combine stir casting with supplementary treatments to overcome challenges such as structural heterogeneity, poor wettability, porosity, and non-uniform particle dispersion, which otherwise degrade the performance of the final composites [15–17]. Particularly effective is the integration of stir casting with ultrasonic treatment, where acoustic vibrations facilitate particle deagglomeration, improve dispersion in the melt, and strengthen interfacial bonding between the matrix and reinforcement [18,19]. Vacuum-assisted casting has also shown benefits by reducing gas entrapment and suppressing pore formation, thereby enhancing the density and homogeneity of the composites [20,21]. Further improvements can be obtained through the combination of stir casting with post-casting deformation or forming techniques, including rolling [22,23], forging [24], and related processes, which refine the grain structure, homogenize particle distribution, and eliminate casting defects, ultimately leading to substantial strengthening. Casting–forming integration, in fact, constitutes the technological basis of most modern metallurgical production chains. In this context, growing attention has recently been devoted to processes operating under complex stress–strain conditions, as they allow for large plastic deformations accompanied by pronounced shear components [25–27]. Such regimes promote grain refinement via dynamic recrystallization and substructure evolution [28–30]. Among these, radial-shear rolling (RSR) is of particular interest, as it combines the advantages of conventional rolling with the generation of intense shear fields [31,32]. Nevertheless, systematic studies on the influence of RSR on the microstructure and properties of cast AMCs remain scarce, limiting the current understanding of the mechanisms responsible for their strengthening and performance.

Regarding the choice of matrix material, both pure aluminum [33] and a wide range of aluminum alloys [34–36] have been employed for reinforcement with either conventional ceramic phases such as Al_2O_3, TiB_2, B_4C, SiC, WC, TiC, and Si_3N_4, or waste-derived reinforcements [37,38]. The latter not only help to reduce composite production costs through the utilization of secondary resources, but also contribute to addressing critical environmental challenges associated with industrial and municipal waste management. Among ceramic reinforcements, titanium diboride (TiB_2) has received particular attention due to its unique combination of properties, including high hardness, tensile strength (~373 MPa), high melting point (~3230 °C), and relatively low density (4.52 g/cm^3) [39]. A further advantage of TiB_2 is the feasibility of in situ particle formation via reactions between titanium-containing precursors (e.g., K_2TiF_6 and KBF_4) and the aluminum melt, which yields fine, uniformly distributed particles with strong interfacial bonding and reduced casting defects [40]. Moreover, combining TiB_2 with other ceramic phases in hybrid composites [41,42] enables the design of materials with tailored multifunctional performance, expanding their potential applications in both structural and functional components.

Building on the above considerations, this study explores the experimental fabrication of Al6060-based aluminum composites reinforced ex situ with 5–10 μm TiB_2 particles via stir casting combined with ultrasonic treatment, which promotes improved particle dispersion

and strong interfacial bonding. To further enhance the mechanical properties and achieve a homogeneous microstructure, the composites were subsequently processed by radial-shear rolling (RSR), a technique capable of introducing intensive shear deformation and stimulating dynamic recrystallization. The novelty of this work lies in the integrated application of stir casting, ultrasonic treatment, and RSR to Al6060/TiB_2 composites, along with the experimental investigation of the role of RSR in tailoring the structure and performance of cast AMCs—a subject that remains scarcely explored in the literature. This combined approach enables the production of composites with superior strength, density, and particle distribution uniformity, thereby broadening their potential for applications in aerospace, automotive, and other advanced engineering sectors.

2. Materials and Methods

2.1. Raw Materials

For this study, the Al6060 aluminum alloy was selected as the matrix material. Rectangular specimens with dimensions of 3 × 30 × 160 mm were cut from commercially available Al6060 plates supplied by Metall-Komplekt LLP (Karaganda, Kazakhstan). The nominal chemical composition of the alloy is provided in Table 1.

Table 1. Chemical composition of Al6060 alloy (wt%).

Mg	Si	Mn	Fe	Cu	Zn	Ti	Others	Al
0.35–0.50	0.30–0.60	≤0.10	0.10–0.30	≤0.10	≤0.15	≤0.10	≤0.15	97.65–99.35

Titanium diboride (TiB_2) particles with a purity of 99.5%, gray–black in color and with a nominal particle size range of 5–10 μm, were used as the reinforcing phase. These particles were procured from Luoyang Tongrun Info Technology Co., Ltd. (Luoyang, China). The morphology, particle size distribution, chemical composition, and phase purity of TiB_2 were characterized using scanning electron microscopy (SEM), energy-dispersive spectroscopy (EDS), and X-ray diffraction (XRD), respectively. Figure 1 presents representative SEM micrographs of the TiB_2 particles, their XRD pattern with the characteristic peaks corresponding to TiB_2, the particle size distribution, and the elemental composition obtained by EDS.

The SEM observations revealed that the TiB_2 particles exhibit predominantly irregular, angular morphologies with a rough surface texture and a wide variation in size. The particle size distribution confirmed that the majority of particles fall within the range of 5–10 μm, with an average size of 6.59 ± 0.57 μm. The XRD pattern verified the presence of a single TiB_2 phase without detectable secondary impurities. The main diffraction peaks were consistent with the reference PDF database, confirming the high phase purity of the powder. EDS analysis further identified titanium (Ti) and boron (B) as the principal elements, with contents close to the stoichiometric composition of TiB_2 (Ti ≈ 67.65 ± 0.80 wt% and B ≈ 27.28 ± 0.22 wt%). A minor carbon signal (C ≈ 5.07 ± 0.18 wt%) was attributed to surface contamination introduced during analysis.

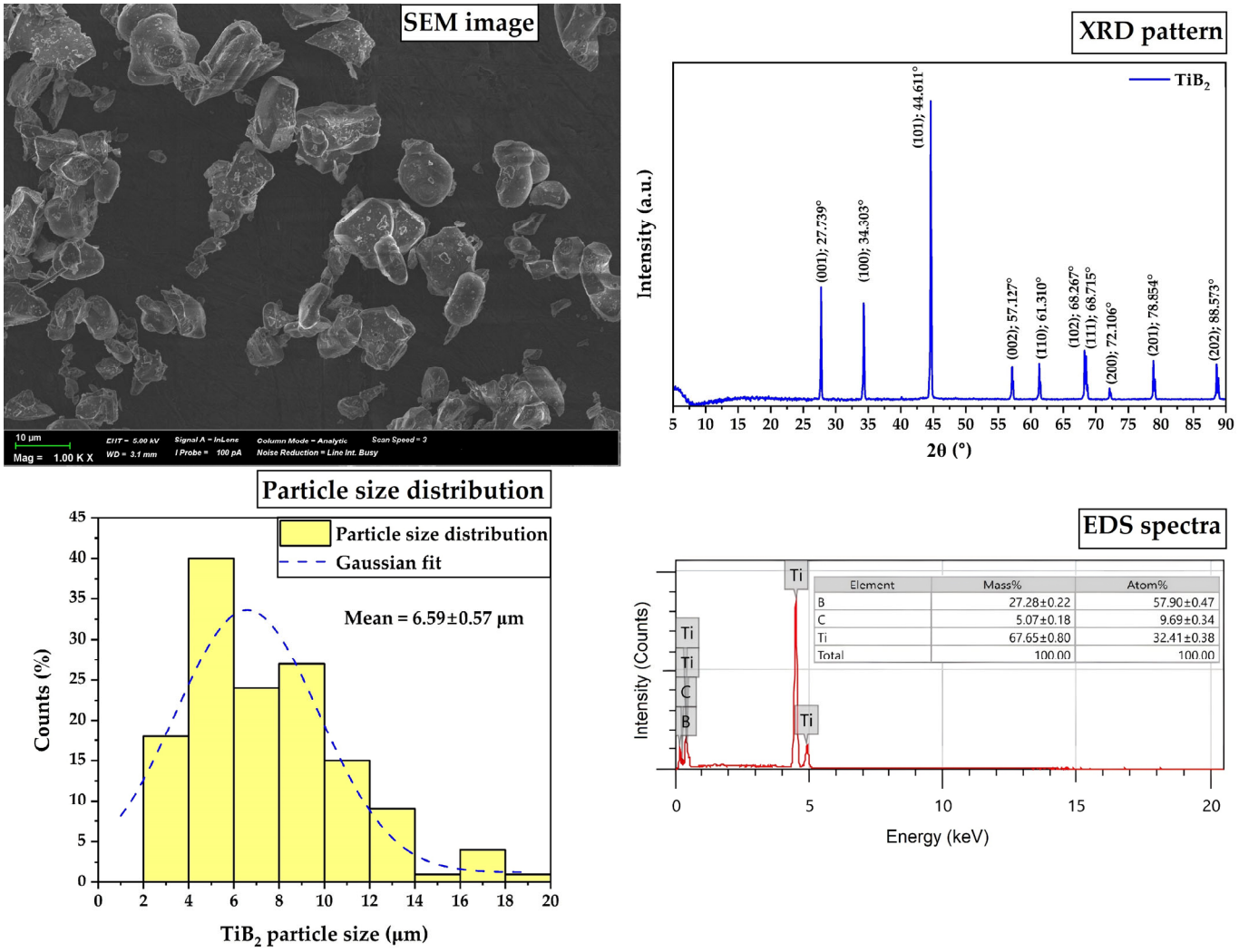

Figure 1. SEM morphology, XRD pattern, size distribution, and EDS spectra of TiB_2 powders used for aluminum reinforcement.

2.2. Fabrication of Composite

A schematic illustration of the fabrication process for the Al6060/TiB_2 composites is shown in Figure 2. To facilitate loading into a graphite crucible with a diameter of 84 mm, the Al6060 matrix plates were pre-cut into specimens of 3 × 30 × 160 mm, thoroughly cleaned, and weighed in accordance with the nomenclature presented in Table 2. The required amounts of TiB_2 powder were also weighed according to this scheme. To minimize the temperature difference between the molten metal (750 °C) and the reinforcing particles, both the aluminum with crucible and the TiB_2 powder were preheated in a PM-5 muffle furnace (Plavka.Pro, Korolev, Russia) to 500 °C at a relatively slow heating rate of 3.75 °C/min. This procedure prevented particle agglomeration caused by sintering at higher heating rates and ensured the removal of residual moisture from both the reinforcement and the crucible.

Table 2. Nomenclature of the fabricated materials.

Nomenclature	Al6060 (wt%)	TiB_2 (wt%)
Al6060–C (cast)	100	0
Al6060–R (rolled)	100	0
Al6060/TiB_2–C (cast)	98	2
Al6060/TiB_2–R (rolled)	98	2

Figure 2. Schematic representation of the fabrication route for Al6060/TiB_2 composites using stir casting combined with ultrasonic treatment and subsequent radial-shear rolling (RSR).

Figure 3 presents the ultrasonically assisted stir casting setup and the radial-shear rolling (RSR) mini mill available at Karaganda Industrial University, which were employed in this study for producing the cast and subsequently rolled composites, respectively. The Al6060 alloy in a graphite crucible was melted in a JC-S-220-4 electric resistance furnace (Zibo JC Eco-Tech Co., Ltd., Zibo, China) at 750 ± 10 °C. To remove dissolved hydrogen and reduce gas porosity, argon was purged through the melt at a flow rate of 2 L/min. The TiB_2 particles were then gradually introduced into the vortex of the melt, which was generated by a four-blade steel impeller coated with graphite paste and operated at ~600 rpm for 10 min. The melt temperature was continuously monitored using a K-type chromel–alumel thermocouple.

After mechanical stirring, the crucible with the melt was rapidly transferred to the working zone of a BR-12NFT-80/300 electric resistance furnace (Henan Dming Technology Co., Ltd., Luohe, China), where ultrasonic treatment was carried out using a JH-LRT30 ultrasonic system (Hangzhou Precision Machinery Co., Ltd., Hangzhou, China). A titanium-alloy ultrasonic probe was immersed into the melt and operated at 20.5–20.7 kHz for 15 min to suppress particle clustering and improve particle–matrix wetting [18,19,33,37]. The

ultrasonically treated melt was then poured into a preheated (450 °C) seven-channel steel mold (Ø25 × 220 mm per channel) and allowed to cool in air until solidification was complete and room temperature was reached. From each casting batch, 5–6 composite billets were obtained, with the upper sections containing external shrinkage removed prior to further processing.

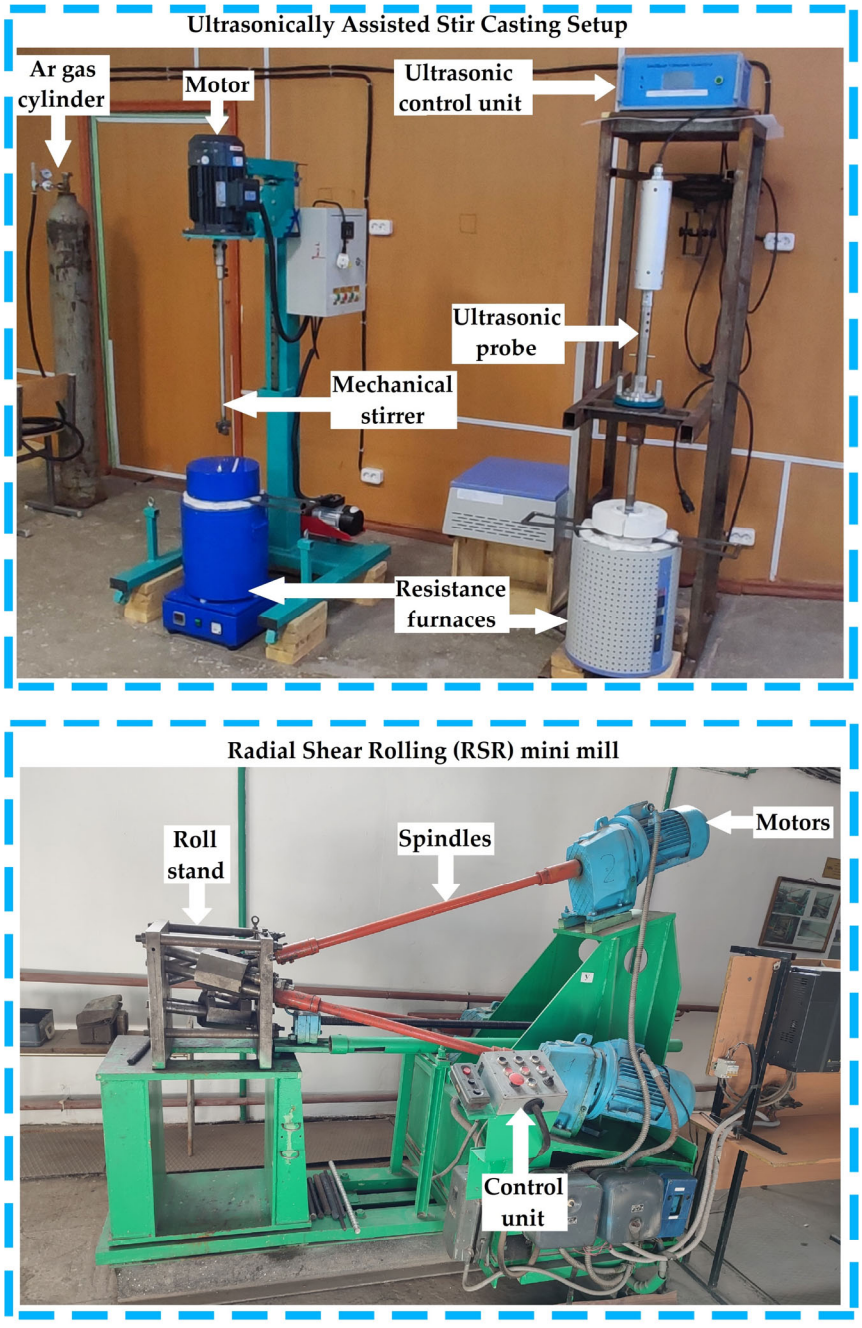

Figure 3. Experimental facilities: ultrasonically assisted stir casting setup and radial-shear rolling (RSR) mini mill employed in this study.

The cast billets with an initial diameter of 25 mm were subjected to warm radial-shear rolling after preheating at 200 °C for 15 min, using the RSR mini mill (Figure 3). Rolling was carried out in four passes to achieve a final diameter of 16 mm (Ø25 mm → Ø22.4 mm → Ø20 mm → Ø17.9 mm → Ø16 mm), corresponding to a total area reduction of 59% and a true strain of ~0.9. The three rolls of the mill were positioned symmetrically at 120° intervals around the rolling axis. The rolling process was conducted at a roll rotation

speed of 100 rpm, with a constant feed angle of 20° and a tilt angle varying from 10° to 7°, following the recommendations in [43].

2.3. Material Characterization

To evaluate the microstructure and mechanical properties of the Al6060/TiB_2 composites after casting and RSR, different types of specimens were prepared (Figure 4).

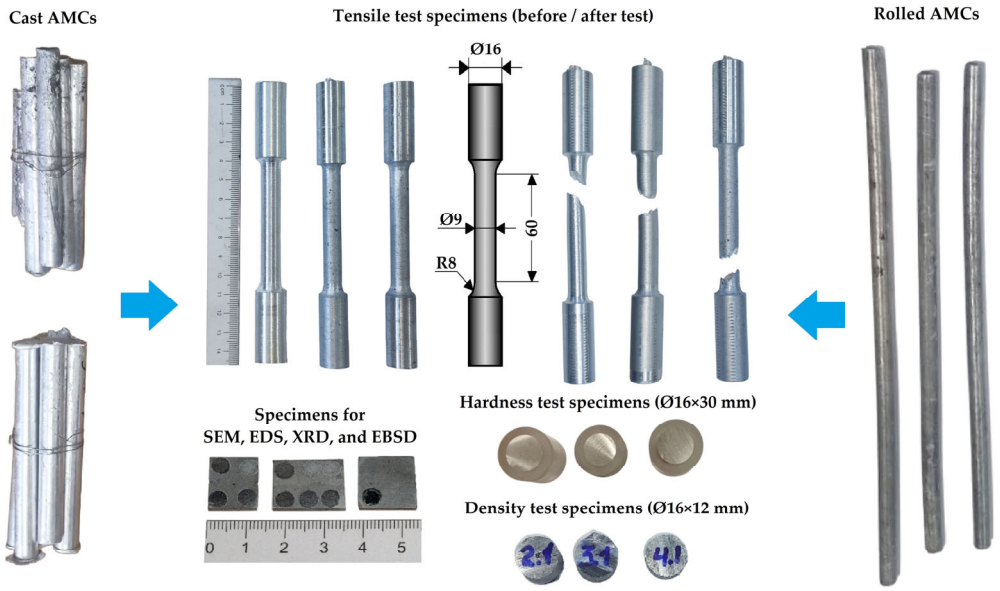

Figure 4. Representative specimens prepared for tensile testing, microhardness measurements, density determination, and microstructural and phase characterization by SEM, EDS, XRD, and EBSD.

Tensile test specimens were machined into a dog-bone geometry (gauge diameter 9 mm, gauge length 60 mm) in accordance with ASTM E8 standards [44]. For each material condition, three specimens were tested to ensure reproducibility. The tests were carried out on a WDW-100 kN universal testing machine (Jinan Xinluchang Testing Machine Co., Ltd., Jinan, China) at a constant crosshead speed of 1 mm/min, corresponding to an average strain rate of ~10^{-3} s^{-1}, until specimen failure at room temperature. Based on the test results, the yield strength (YS), ultimate tensile strength (UTS, MPa), and elongation (%) were determined.

For hardness measurements, cylindrical samples with a diameter of 16 mm and a height of 30 mm were used. For each condition, at least five indentations were performed at different locations on each specimen to account for possible microstructural heterogeneity. The hardness of the composites was evaluated using the microindentation method in accordance with ASTM E384 [45] on an HVT-1000A microhardness tester (Laizhou Laihua Testing Instrument Factory, Laizhou, China) equipped with a diamond pyramid indenter with an included angle of 136° between opposite faces. Cylindrical specimens with a diameter of 16 mm and a height of 30 mm were used for the tests. Prior to measurement, the sample surfaces were sequentially ground with SiC abrasive papers of decreasing grit size (from 400 to 1500), followed by final polishing on cloth disks with an alumina suspension (1–0.3 µm) until a mirror-like finish was achieved. After polishing, the specimens were cleaned with ethanol and dried with compressed air. For each specimen, a minimum of five indentations were performed at different locations. The Vickers microhardness (HV0.2) was calculated using Equation (1), based on the average diagonal length d of the indentation produced under a load of 0.2 kgf (~1.96 N) applied for 15 s:

$$HV0.2 \approx 1.8544F/d^2 \approx 0.18544d^{-2} \quad (1)$$

The density of the materials was determined using the hydrostatic weighing method [46] with an MH-300A electronic densitometer (Shenzhen Omena Technology Co., Ltd., Shenzhen, China). Cylindrical specimens with a diameter of 16 mm and a height of 12 mm were prepared for testing, with five specimens produced for each composition. Prior to measurement, the samples were carefully cleaned of surface contaminants. The mass of each specimen was recorded first in air (m_{air}) and then in distilled water (m_{water}) at a temperature of 23 ± 1 °C. The density of water at this temperature, taken from [47], was ϱ_{water} = 0.9975412 g/cm^3. The densitometer automatically recorded the masses with an accuracy of 0.01 g. The theoretical density of the composites (ϱ_{th}) was calculated using the rule of mixtures according to Equation (2):

$$\varrho_{th} = \varrho_{Al} \times wt\%_{Al} + \varrho_r \times wt\%_r \quad (2)$$

where ϱ_{Al} is the density of the aluminum matrix (~2.71 g/cm^3), ϱ_r is the density of the reinforcement (~4.52 g/cm^3), and $wt\%_{Al}$ and $wt\%_r$ are the weight fractions of the matrix and reinforcement, respectively, as listed in Table 2. The experimental density (ϱ_{exp}) was determined according to Archimedes' principle using Equation (3):

$$\varrho_{exp} = [m_{air}/(m_{air} - m_{water})] \times \varrho_{water} \quad (3)$$

The discrepancy between experimental and theoretical density was used to estimate the porosity of the materials according to Equation (4):

$$\text{Porosity (\%)} = [1 - (\varrho_{exp}/\varrho_{th})] \times 100 \quad (4)$$

Microstructural and phase characterization of the composites was carried out using scanning electron microscopy (SEM), energy-dispersive spectroscopy (EDS), X-ray diffraction (XRD), and electron backscatter diffraction (EBSD). Microstructural images were obtained with a JSM-IT200 scanning electron microscope (Jeol, Tokyo, Japan) equipped with a secondary electron detector, operated at an accelerating voltage of 20 kV. Elemental analysis was performed using the built-in EDS detector.

Specimens were sectioned along the diametral plane of the billets using a Brilliant 220 precision cutting machine (ATM Qness GmbH, Mammelzen, Germany), with the thickness of each slice being 3 mm. The samples were then hot-mounted in carbon-containing Struers PolyFast resin (Struers ApS, Ballerup, Denmark) using a Citopress-5 mounting press (Struers, Cleveland, OH, USA). Grinding was performed on a Saphir 520 automatic grinding–polishing machine (ATM Qness GmbH, Mammelzen, Germany) with SiC-based abrasive papers of progressively finer grit sizes: P320 → P500 → P800 → P1200 → P2000. Polishing was carried out on cloth disks using diamond suspensions with particle sizes of 9 → 3 → 1 µm, followed by final polishing with an Eposil M suspension (ATM Qness GmbH, Mammelzen, Germany) containing particles of 0.06 µm at pH = 9.5.

Phase analysis was conducted via XRD using a Rigaku SmartLab diffractometer (Rigaku Corporation, Tokyo, Japan) with monochromatic Cu Kα radiation (λ = 1.5406 Å). The scans were performed in the 2θ range of 5–90° with a step size of 0.05°.

The microstructural examination of samples after RSR was further complemented by EBSD analysis, which has proven effective in similar studies [48–50]. EBSD mapping was performed using a Thermo Fisher Scientific Helios 5 UX SEM (Waltham, MA, USA), yielding crystallographic orientation maps (Inverse Pole Figure, IPF) in the RD–ND (rolling direction—normal direction, i.e., longitudinal section) and TD–ND planes (transverse direction—normal direction, i.e., transverse section).

3. Results and Discussion

3.1. EDS and XRD

Figure 5 presents the results of the EDS analysis of as-cast Al6060–C and Al6060/TiB_2–C samples, including the original SEM image and the corresponding elemental distribution maps. The EDS spectrum and maps for the Al6060–C alloy confirm the presence of the main alloying elements, Mg and Si. In both materials, the measured Al content appears underestimated due to the contribution of surface C and O [51,52]. The elevated C signal in both cases is consistent with the use of a graphite crucible: diffusion and/or reaction of the melt with carbon may lead to surface carburization of the ingot and/or the formation of carbon-rich inclusions, subsequently detected by EDS.

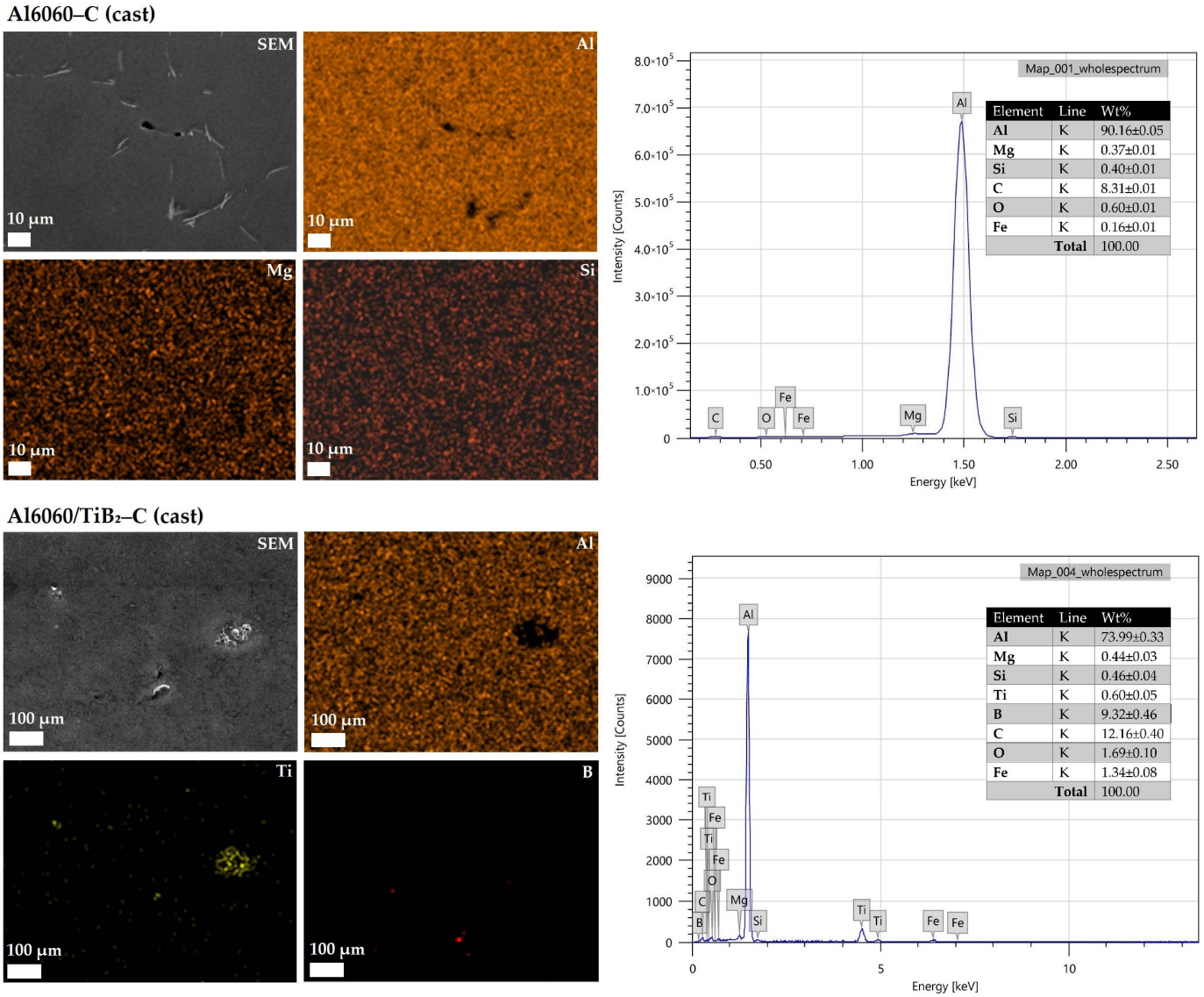

Figure 5. SEM–EDS analysis of cast Al6060–C and Al6060/TiB_2–C composites, showing micrographs, elemental distribution maps, and representative spectra.

The EDS data for the Al6060/TiB_2–C sample qualitatively confirm the presence of Ti- and B-containing regions. The Ti and B signals are spatially correlated (coincident regions), consistent with the presence of TiB_2 particles embedded in the aluminum matrix after casting. In this case, the Ti/B maps serve as a reliable indicator of the reinforcing phase [53,54]. These EDS observations are in agreement with the XRD results, where both

cast and rolled samples exhibit characteristic peaks of Al and TiB_2 (Figure 6). It should be emphasized, however, that the sensitivity of the employed methods imposes limitations: thin interfacial reaction layers or amorphous/oxide films of low volume fraction may not be detected by either XRD or EDS. Therefore, the absence of such products in the results should be considered qualitative and constrained by the detection limits of the techniques used.

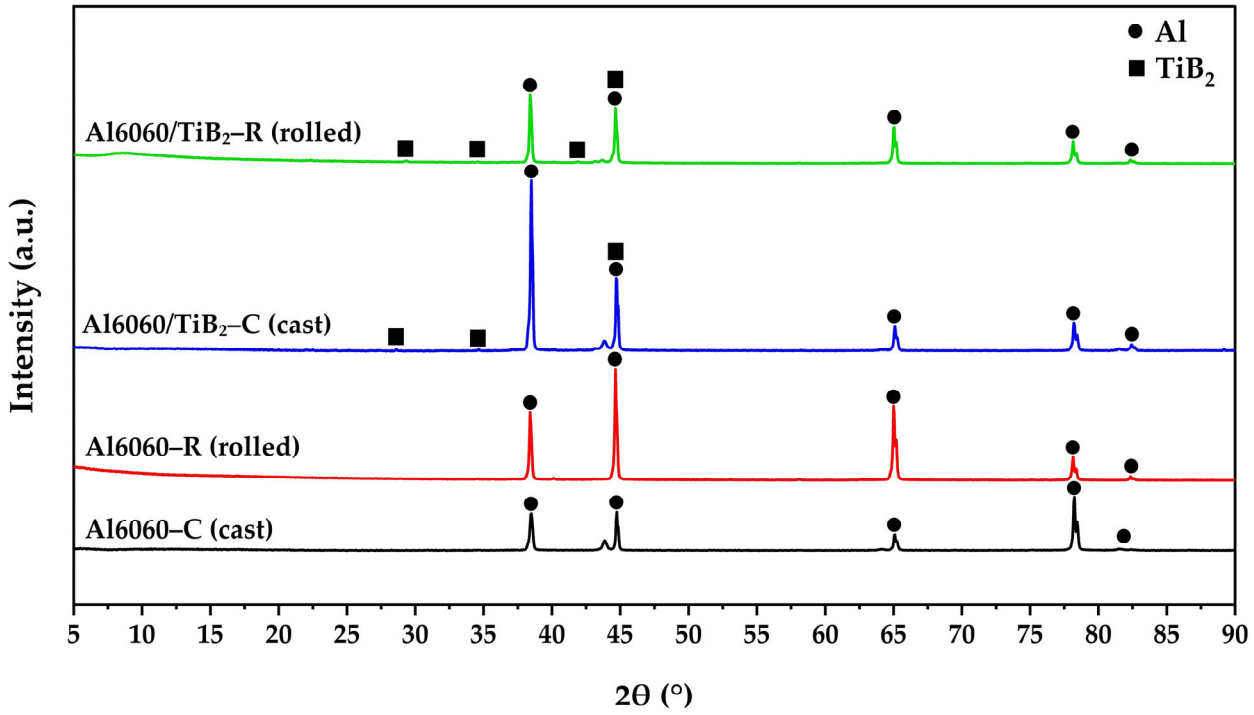

Figure 6. XRD diffractograms of Al6060 and Al6060/TiB_2 in as-cast and RSR-processed conditions.

For the as-cast Al6060 alloy, the diffraction pattern reveals the strong reflections corresponding to the aluminum phase. The most prominent peaks are observed at 2θ = 38.443°, 44.722°, 65.072°, and 78.232°, corresponding to the {111}, {200}, {220}, and {311} planes, respectively. Among these, the (200) reflection exhibited the highest intensity, followed by (111) and (220), in agreement with standard PDF no. 01-072-3440 [55,56]. No additional phases were detected for Al6060–C, which is expected given the relatively narrow range of alloying elements in the Al6060 composition.

After RSR, the Al6060–R samples retained the same aluminum peaks as the as-cast alloy; however, their absolute intensities increased significantly due to enhanced crystallinity and reduced porosity. The relative intensities also changed: the (200) reflection remained the most intense, followed by (220), while the (111) peak, although higher than in the as-cast state, remained less intense than both (200) and (220). This redistribution of intensities reflects the development of deformation-induced texture, consistent with FCC aluminum alloys subjected to severe plastic deformation [57,58]. Thus, XRD analysis reveals not a change in phase composition, but rather the evolution of crystallographic texture in the aluminum lattice induced by RSR.

In the diffraction patterns of the Al6060/TiB_2–C and Al6060/TiB_2–R composites, additional peaks are clearly observed at 2θ = 27.681°, 34.624°, and 41.840° (PDF no. 000-35-0741), which are identified as TiB_2 [59,60]. Their moderate intensity is consistent with the relatively low content of the reinforcing phase (2 wt.%). Importantly, the TiB_2 peaks exhibit relatively sharp profiles, indicating the preservation of the original crystalline structure and the absence of significant disordering during contact with the melt. This is consistent

with the SEM–EDS data, where TiB_2 particles are observed as discrete inclusions without visible reaction layers.

No characteristic reflections of intermetallics such as Al_3Ti ($2\theta \approx 39.5^\circ$, 40.6°) or AlB_2 ($2\theta \approx 42^\circ$) were detected in the diffractograms. This indicates that, under the present experimental conditions, thermodynamically feasible reactions leading to TiB_2 decomposition and the formation of new phases did not occur to a detectable extent. Possible reasons include: (i) the high chemical stability of TiB_2, (ii) the relatively short residence time of particles in the melt, and (iii) their low volume fraction, which reduces the probability of significant interfacial reactions. Thus, the XRD results confirm that the reinforcing phase retains its crystalline integrity and discrete morphology when transferred from the powder state into the cast composite.

For the rolled composite, TiB_2 peaks remain at the same positions but become sharper and more pronounced. This can be attributed to the more uniform distribution of particles throughout the matrix after RSR, as well as the elimination of pores, which improves diffraction conditions. In addition, the aluminum matrix exhibits a redistribution of peak intensities, indicating texture formation. Notably, the relative intensity of the TiB_2 reflection at $2\theta = 41.840^\circ$ increases, most likely due to the preferred orientation of particles along the rolling direction. While TiB_2 particles do not deform plastically, they can rotate and redistribute within the plastically deforming aluminum matrix.

A key issue in the development of Al/TiB_2 composites concerns the possible formation of reaction products at the particle–matrix interface. According to the literature [61–63], at temperatures above 900 °C and under prolonged holding, partial dissociation of TiB_2 may occur, releasing Ti and B and leading to the formation of Al_3Ti intermetallics and aluminum borides. In the present study, however, the melt temperature did not exceed 750 ± 10 °C, and the residence time of the particles in the melt was limited to 10–15 min. These conditions are clearly insufficient for the thermodynamic and kinetic initiation of TiB_2 decomposition reactions. Therefore, the XRD analysis confirms that the composites remain two-phase systems (Al + TiB_2), with no additional compounds detected within the resolution limits of the method.

3.2. SEM and EBSD

SEM micrographs (Figure 7) reveal the classical contrast between the cast and deformed states. In the as-cast Al6060–C sample, a coarse dendritic morphology is observed, with individual grains reaching several tens of micrometers in size, featuring well-defined boundaries and localized porosity. In contrast, RSR processing induces pronounced microstructural recrystallization and structural homogenization (Al6060–R). The introduction of ~2 wt.% TiB_2 particles further modifies this picture. SEM images show that the reinforcing particles are distributed relatively uniformly throughout the matrix and, unlike in conventional casting without external treatment, do not form extended agglomerates. This effect is a direct consequence of ultrasonic melt treatment, which is known to disintegrate particle clusters and promote aluminum wetting [64–66]. The average particle size, provided by the supplier and confirmed by morphological analysis, is 6.59 ± 0.57 μm (Figure 1). Visual inspection of the SEM micrographs indicates that the characteristic interparticle spacing within the matrix is on the order of 15–25 μm, which is consistent with expectations for the given concentration and powder size. This suggests a sufficiently homogeneous distribution, whereby a substantial fraction of the matrix volume is affected by the reinforcing phase despite its minor overall fraction.

The particle–matrix interface is also of particular importance. At higher magnification, no distinct interlayers or reaction products are observed at the interface. The contact appears clean and well-bonded, consistent with the XRD results, which revealed no reflections of

new intermetallic phases such as Al_3Ti. Such an interface character suggests good adhesion and, consequently, the ability of the particles to efficiently transfer load from the matrix during tensile loading. Only in isolated cases are thin microgaps or localized contrast regions detected around the particles, most likely associated with crystallization stresses or mismatch in thermal expansion. However, the fraction of such defects is negligible, and they are not expected to critically affect the composite integrity.

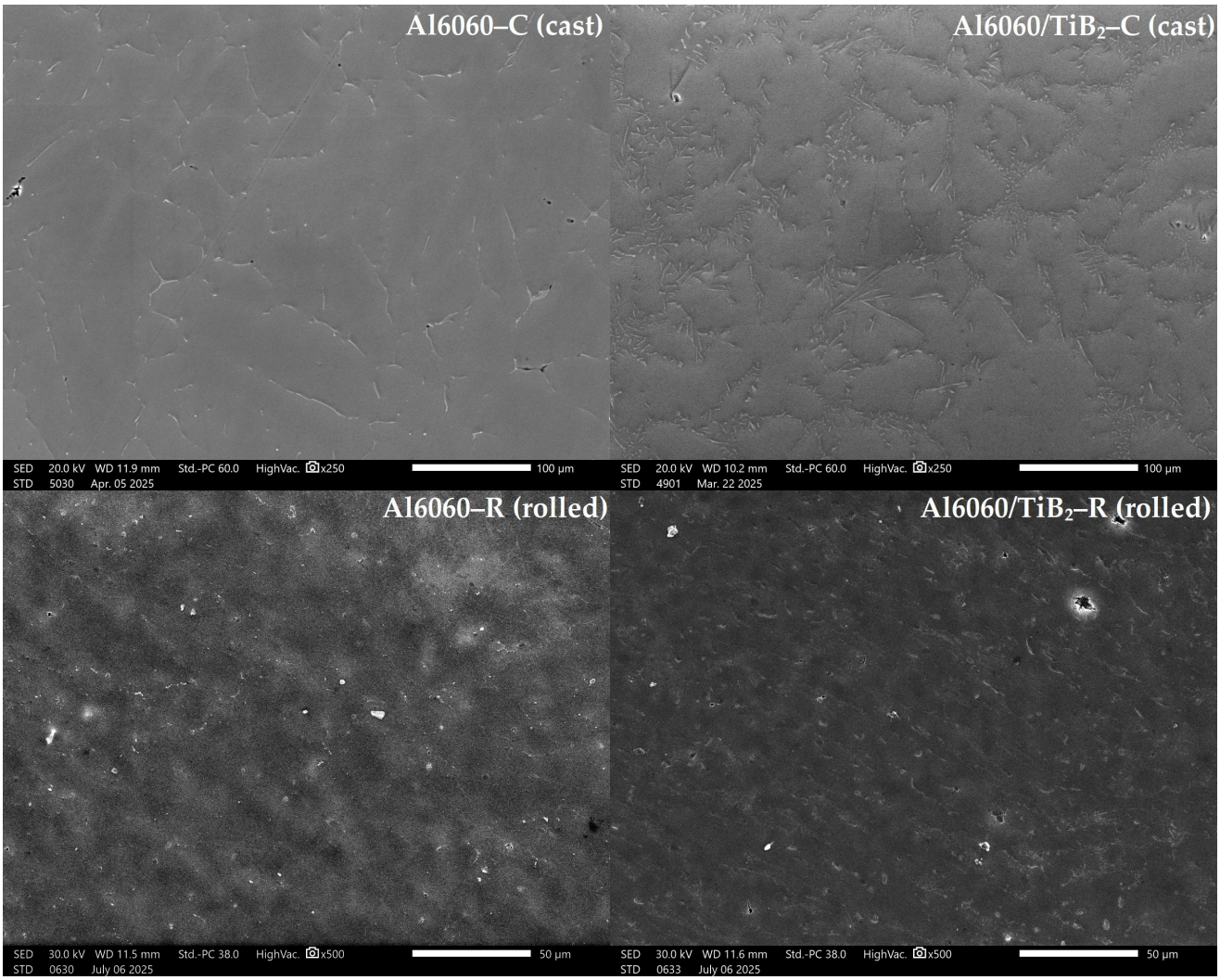

Figure 7. SEM micrographs of cast and rolled Al6060 and Al6060/TiB_2 samples.

A comparison of cast and rolled samples highlights several fundamental differences. Following RSR, the cast structure undergoes significant grain refinement. In SEM images of the rolled specimens, grains appear markedly smaller and elongated along the rolling direction. Casting-induced porosity is largely absent in the rolled material, as most pores are either closed, fragmented, or dissolved into the matrix, consistent with previous findings [67–69]. Simultaneously, TiB_2 particles undergo partial redistribution. Whereas in the cast state they are arranged in a predominantly random manner, after RSR they exhibit partial alignment and a tendency to orient along the rolling direction. Some particles are incorporated into newly formed grain boundaries, which further contributes to the stabilization of the refined structure.

EBSD orientation maps (Figure 8) provide a detailed insight into the effect of RSR and the role of 2 wt.% TiB_2 on the texture and grain structure. After radial-shear rolling, the Al6060–R alloy exhibits pronounced anisotropy of the grain structure. In the RD–ND

plane, elongated band-like grains are clearly visible, alternating with larger recrystallized regions. The average equivalent grain diameter in this state is about 12–15 μm, while local areas with coarser grains up to 30–35 μm are still preserved. The TD–ND projection further reveals extended blocks of uniform orientation, confirming incomplete dynamic recrystallization: part of the structure still retains features of the cast morphology.

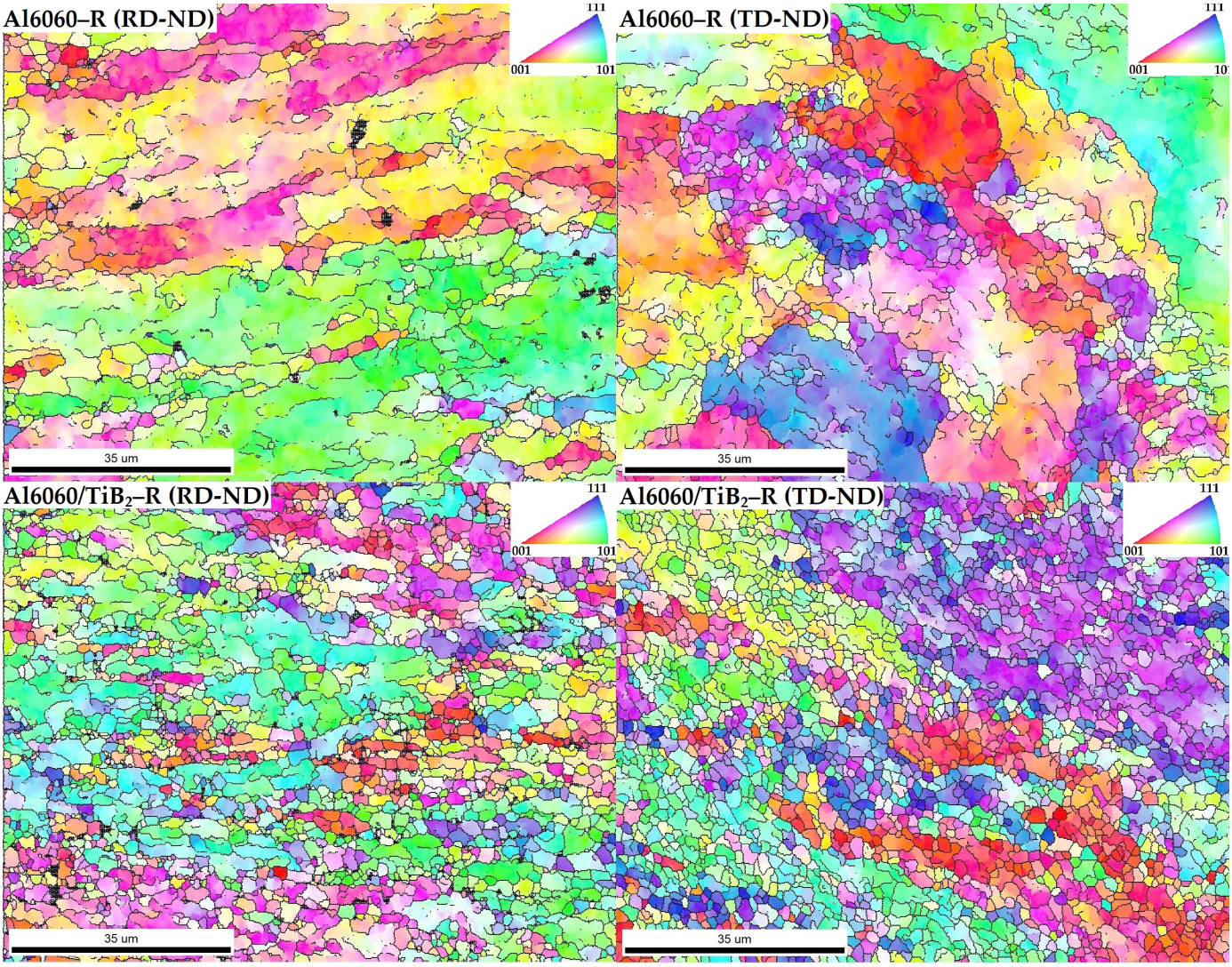

Figure 8. EBSD orientation maps of the RD–ND and TD–ND planes of rolled Al6060–R and Al6060/TiB_2–R samples.

The addition of 2 wt.% TiB_2 markedly alters the microstructure. In the Al6060/TiB_2–R samples, the grain structure becomes significantly finer and more homogeneous. In both RD–ND and TD–ND maps, a uniform mosaic of small, differently oriented grains is observed. The average equivalent grain size decreases to 4–6 μm, while the maximum grain size does not exceed 10–12 μm. The presence of TiB_2 particles promotes both enhanced nucleation during dynamic recrystallization and effective suppression of grain growth via the Zener pinning effect [70,71].

Furthermore, EBSD maps demonstrate a weakening of the rolling texture: the color distribution of grains in Al6060/TiB_2–R is noticeably more heterogeneous than in Al6060–R, indicating reduced texture anisotropy. Thus, a comparison of the two EBSD series shows that while RSR alone induces grain refinement in Al6060, it also retains marked anisotropy and partial deformation texture. The introduction of TiB_2 provides an additional strength-

ening effect through the combined action of grain refinement and texture weakening [72,73]. These observations are consistent with the SEM results (Figure 7), which also showed that TiB_2 particles, after stir casting and ultrasonic treatment, are relatively uniformly dispersed and well-integrated into the aluminum matrix. Together, these findings explain the expected increase in yield strength and hardness in Al6060/TiB_2–R compared to Al6060–R, along with a reduction in anisotropy of mechanical properties.

3.3. Mechanical Properties

The results of mechanical testing (Figure 9) clearly demonstrate that the combination of ultrasonically assisted stir casting and subsequent RSR leads to a substantial enhancement of strength and hardness, while also influencing ductility. In the as-cast state, the Al6060–C alloy exhibits relatively low yield strength (YS = 61.7 MPa) and ultimate tensile strength (UTS = 103.3 MPa), with an elongation to fracture of about 19.5%. This performance is consistent with its coarse-grained dendritic structure, the presence of shrinkage porosity, and insufficient intergranular cohesion, as previously observed in SEM images.

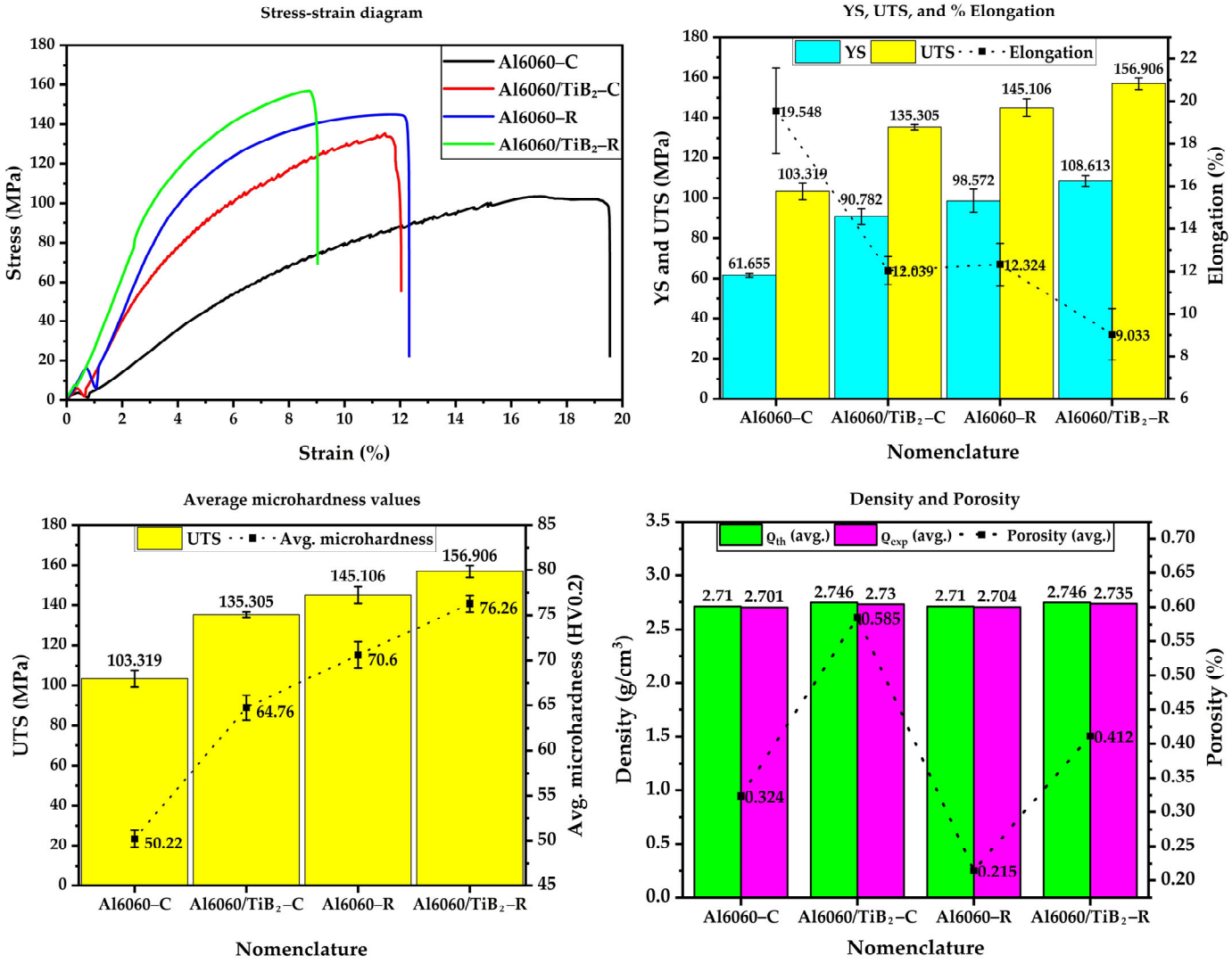

Figure 9. Comparison of mechanical properties of the investigated samples.

The addition of 2 wt.% TiB_2 to the cast alloy (Al6060/TiB_2–C) increases strength: YS rises to 90.8 MPa and UTS to 135.3 MPa, while elongation decreases to 12.0%. The strengthening effect is attributed to dispersed TiB_2 particles impeding dislocation motion,

whereas the reduced ductility is associated with local stress concentrations around particles and residual porosity (~0.59% compared to ~0.32% in Al6060–C).

After radial-shear rolling (Al6060–R), mechanical performance is significantly improved: YS increases to 98.6 MPa and UTS to 145.1 MPa, driven by grain refinement (average grain size ~12–15 μm, Figure 8) and reduced porosity (~0.21%). Elongation remains at a moderate 12.3%, indicating retained ductility owing to partial recrystallization.

The most outstanding properties are observed in the rolled composite (Al6060/TiB_2–R): YS reaches 108.6 MPa, UTS rises to 156.9 MPa, and the average microhardness achieves 76.3 HV0.2 (compared to 50.2 HV0.2 in the as-cast Al6060–C). This superior combination results from multiple strengthening mechanisms acting simultaneously: grain refinement (Hall–Petch mechanism [74,75]), dispersion strengthening by TiB_2 particles (Orowan mechanism [76,77]), and increased density after RSR, where porosity is reduced to ~0.14%. However, ductility further decreases to 9.0%, reflecting the limited ability of the matrix to deform plastically in the presence of rigid particles.

In summary, the combination of stir casting, ultrasonic treatment, and RSR enables a significant improvement in the strength and hardness of Al6060/TiB_2 composites compared with the as-cast state. While in the unreinforced Al6060 alloy the improvement is mainly due to grain refinement and densification, in the composite an additional contribution from dispersion strengthening by TiB_2 allows achieving UTS values above 156 MPa and hardness of ~76 HV0.2, while retaining acceptable ductility (~9%).

4. Conclusions

In this study, the structure and mechanical properties of Al6060/TiB_2 aluminum matrix composites fabricated by ultrasonically assisted stir casting followed by radial-shear rolling (RSR) were experimentally investigated. The main findings can be summarized as follows:

1. Microstructure. Ultrasonic treatment of the melt during stir casting ensured a uniform distribution of TiB_2 particles (~2 wt.%) within the aluminum matrix, preventing the formation of pronounced agglomerates and reaction layers at the particle–matrix interface. Subsequent RSR further refined the grain structure (reducing the average size to 4–6 μm in Al6060/TiB_2–R compared to 12–15 μm in Al6060–R) and reduced porosity relative to the as-cast state.
2. Phase composition. XRD and EDS analyses confirmed that the reinforcing phase is preserved as discrete TiB_2 particles without the formation of intermetallic compounds such as Al_3Ti or AlB_2. In rolled samples, enhanced texture effects of the aluminum matrix were observed: the relative intensities of the main Al reflections changed, with (200) and (220) becoming more pronounced than (111), consistent with deformation-induced texture evolution. Partial alignment of TiB_2 particles along the deformation direction was also observed.
3. Mechanical properties. The as-cast Al6060–C alloy exhibits low strength (UTS~103 MPa, YS~62 MPa) but high ductility (~19.5%). The addition of 2 wt.% TiB_2 in the as-cast condition (Al6060/TiB_2–C) increases strength (UTS~135 MPa, YS~91 MPa) but reduces elongation to ~12%. RSR of the unreinforced alloy (Al6060–R) improves strength (UTS~145 MPa, YS~99 MPa) through grain refinement and defect reduction, while retaining satisfactory ductility (~12%). The rolled composite (Al6060/TiB_2–R) demonstrates the highest performance, with UTS~157 MPa, YS~109 MPa, microhardness ~76 HV0.2, and ductility of ~9%. These improvements are attributed to a combined effect of grain refinement (Hall–Petch mechanism), dispersion strengthening by TiB_2 particles (Orowan mechanism), as well as reduced porosity and improved particle distribution uniformity.

In conclusion, the integrated approach combining ultrasonically assisted stir casting and radial-shear rolling represents an effective processing strategy for producing Al6060/TiB_2 aluminum matrix composites with enhanced strength, hardness, and density while maintaining acceptable ductility. The obtained results broaden the potential applications of such materials in aerospace, automotive, and other high-technology industries where an optimal balance of lightweight design and high performance is required.

Author Contributions: Conceptualization, M.A. and I.T.; methodology, M.A., I.T. and N.L.; validation, N.L. and Z.A.; formal analysis, N.L. and Z.A.; investigation, K.N. and S.K.; resources, M.A. and I.T.; data curation, Z.A. and S.K.; writing—original draft preparation, M.A. and I.T.; writing—review and editing, N.L. and K.N.; visualization, Z.A. and S.K.; supervision, M.A.; project administration, M.A.; funding acquisition, M.A. All authors have read and agreed to the published version of the manuscript.

Funding: This research is funded by the Science Committee of the Ministry of Science and Higher Education of the Republic of Kazakhstan (Grant No. AP19677907).

Data Availability Statement: All the relevant data are contained within the article itself. Additional data may be shared by the authors following a reasonable request.

Acknowledgments: The authors express their sincere gratitude to Nursultan Amanzholov (Karaganda Industrial University, Temirtau, Kazakhstan) for valuable assistance in performing the ultrasonically assisted stir casting experiments. Special thanks are extended to Anatoly Kustov (Karaganda Industrial University, Temirtau, Kazakhstan) for his support in conducting the radial-shear rolling processing. The authors also acknowledge Beldeubayev Askhat (Nazarbayev University, Astana, Kazakhstan) for his help with the XRD characterization. During the preparation of this manuscript, the authors used ChatGPT (GPT-5, OpenAI) for assistance in improving the English language style and grammar. The authors have reviewed and edited the content carefully and take full responsibility for the final version of the manuscript.

Conflicts of Interest: The authors declare no conflicts of interest.

References

1. Nartu, M.S.K.K.Y.; Agrawal, P. Additive manufacturing of metal matrix composites. *Mater. Des.* **2025**, *252*, 113609. [CrossRef]
2. Parikh, V.K.; Patel, V.; Pandya, D.P.; Andersson, J. Current status on manufacturing routes to produce metal matrix composites: State-of-the-art. *Heliyon* **2023**, *9*, e13558. [CrossRef] [PubMed]
3. Metal Matrix Composites Market Size, Suppliers to 2033. Available online: https://straitsresearch.com/report/metal-matrix-composites-market (accessed on 20 August 2025).
4. Kar, A.; Sharma, A.; Kumar, S. A Critical Review on Recent Advancements in Aluminium-Based Metal Matrix Composites. *Crystals* **2024**, *14*, 412. [CrossRef]
5. Ujah, C.O.; Kallon, D.V.V. Trends in Aluminium Matrix Composite Development. *Crystals* **2022**, *12*, 1357. [CrossRef]
6. Khalid, M.Y.; Umer, R.; Khan, K.A. Review of recent trends and developments in aluminium 7075 alloy and its metal matrix composites (MMCs) for aircraft applications. *Results Eng.* **2023**, *20*, 101372. [CrossRef]
7. Singh, M.; Garg, H.K.; Maharana, S.; Muniappan, A.; Loganathan, M.K.; Nguyen, T.V.T.; Vijayan, V. Design and Analysis of an Automobile Disc Brake Rotor by Using Hybrid Aluminium Metal Matrix Composite for High Reliability. *J. Compos. Sci.* **2023**, *7*, 244. [CrossRef]
8. Muribwathoho, O.; Msomi, V.; Mabuwa, S. Metal Matrix Composite Fabricated with 5000 Series Marine Grades of Aluminium Using FSP Technique: State of the Art Review. *Appl. Sci.* **2022**, *12*, 12832. [CrossRef]
9. Akbari, T.; Ansari, A.; Rahimi Pishbijari, M. Influence of aluminum alloys on protection performance of metal matrix composite armor reinforced with ceramic particles under ballistic impact. *Ceram. Int.* **2023**, *49*, 30937–30950. [CrossRef]
10. Garg, P.; Jamwal, A.; Kumar, D.; Sadasivuni, K.K.; Hussain, C.M.; Gupta, P. Advance research progresses in aluminium matrix composites: Manufacturing & applications. *J. Mater. Res. Technol.* **2019**, *8*, 4924–4939. [CrossRef]
11. Ramanathan, A.; Krishnan, P.K.; Muraliraja, R. A review on the production of metal matrix composites through stir casting–Furnace design, properties, challenges, and research opportunities. *J. Manuf. Process.* **2019**, *42*, 213–245. [CrossRef]
12. Bhowmik, A.; Kumar, R.; Beemkumar, N.; Kumar, A.V.; Singh, G.; Kulshreshta, A.; Mann, V.S.; Santhosh, A.J. Casting of particle reinforced metal matrix composite by liquid state fabrication method: A review. *Results Eng.* **2024**, *24*, 103152. [CrossRef]

13. Grilo, J.; Carneiro, V.H.; Teixeira, J.C.; Puga, H. Manufacturing Methodology on Casting-Based Aluminium Matrix Composites: Systematic Review. *Metals* **2021**, *11*, 436. [CrossRef]
14. Yadav, P.; Ranjan, A.; Kumar, H.; Mishra, A.; Yoon, J. A Contemporary Review of Aluminium MMC Developed through Stir-Casting Route. *Materials* **2021**, *14*, 6386. [CrossRef]
15. Malaki, M.; Fadaei Tehrani, A.; Niroumand, B.; Gupta, M. Wettability in Metal Matrix Composites. *Metals* **2021**, *11*, 1034. [CrossRef]
16. Negi, A.S.; Shanmugasundaram, T. Hybrid particles dispersion strengthened aluminum metal matrix composite processed by stir casting. *Mater. Today Proc.* **2021**, *39*, 1210–1214. [CrossRef]
17. Yashpal; Sumankant; Jawalkar, C.S.; Verma, A.S.; Suri, N.M. Fabrication of Aluminium Metal Matrix Composites with Particulate Reinforcement: A Review. *Mater. Today Proc.* **2017**, *4*, 2927–2936. [CrossRef]
18. Venkatesh, V.S.S.; Rao, G.P.; Patnaik, L.; Gupta, N.; Kumar, S.; Saxena, K.K.; Sunil, B.D.Y.; Eldin, S.M.; Kafaji, F.H.K.A. Processing and evaluation of nano SiC reinforced aluminium composite synthesized through ultrasonically assisted stir casting process. *J. Mater. Res. Technol.* **2023**, *24*, 7394–7408. [CrossRef]
19. Gudipudi, S.; Nagamuthu, S.; Subbian, K.S.; Chilakalapalli, S.P.R. Enhanced mechanical properties of AA6061-B_4C composites developed by a novel ultra-sonic assisted stir casting. *Eng. Sci. Technol. Int. J.* **2020**, *23*, 1233–1243. [CrossRef]
20. Pethuraj, M.; Uthayakumar, M.; Rajesh, S.; Abdul Majid, M.S.; Rajakarunakaran, S.; Niemczewska-Wójcik, M. Dry sliding wear studies on sillimanite and B_4C reinforced aluminum hybrid composites fabricated by vacuum-assisted stir casting process. *Materials* **2023**, *16*, 259. [CrossRef]
21. Tharanikumar, L.; Mohan, B.; Anbuchezhiyan, G. Enhancing the microstructure and mechanical properties of Si_3N_4–BN strengthened Al–Zn–Mg alloy hybrid nano composites using vacuum assisted stir casting method. *J. Mater. Res. Technol.* **2022**, *20*, 3646–3655. [CrossRef]
22. Luo, Y.; Yi, J.; Chen, M.; Zhou, L.; Zhang, Z.; Huang, Z.; Sun, X.; Zhang, Y.; Wen, L.; Wu, Z. Effect of hot rolling on microstructures and mechanical properties of SiCp/A356 aluminum matrix composites. *J. Mater. Res. Technol.* **2024**, *33*, 1776–1784. [CrossRef]
23. Manokaran, V.; Michael, A.X.; Pazhani, A.; Batako, A. Residual Stress Evolution of Graphene-Reinforced AA2195 (Aluminum–Lithium) Composite for Aerospace Structural Hydrogen Fuel Tank Application. *J. Compos. Sci.* **2025**, *9*, 369. [CrossRef]
24. Purohit, R.; Qureshi, M.M.U.; Kumar, B. Effect of Forging on Aluminum Matrix Nano Composites: A Review. *Mater. Today Proc.* **2017**, *4*, 5357–5360. [CrossRef]
25. Segal, V.; Reznikov, S.V.; Murching, N.; Hammond, V.H.; Kecskes, L.J. Semi-Continuous Equal-Channel Angular Extrusion and Rolling of AA5083 and AZ31 Alloys. *Metals* **2019**, *9*, 1035. [CrossRef]
26. Abishkenov, M.; Ashkeyev, Z.; Mashekov, S.; Akhmetova, G.; Volokitina, I. Investigation of the stress-strain state of balls under deformation in a closed die. *Metalurgija* **2020**, *59*, 559–562.
27. Wang, T.; Zuo, X.; Zhou, Y.; Tian, J.; Ran, S. High strength and high ductility nano-Ni-Al_2O_3/A356 composites fabricated with nickel-plating and equal channel angle semi-solid extrusion (ECASE). *J. Mater. Res. Technol.* **2021**, *13*, 1615–1627. [CrossRef]
28. Abishkenov, M.; Ashkeyev, Z.; Nogaev, K. Investigation of the shape rolling process implementing intense shear strains in special diamond passes. *Materialia* **2022**, *26*, 101573. [CrossRef]
29. Straumal, B.B.; Kulagin, R.; Klinger, L.; Rabkin, E.; Straumal, P.B.; Kogtenkova, O.A.; Baretzky, B. Structure Refinement and Fragmentation of Precipitates under Severe Plastic Deformation: A Review. *Materials* **2022**, *15*, 601. [CrossRef]
30. Abishkenov, M.; Ashkeyev, Z.; Nogaev, K.; Bestembek, Y.; Azimbayev, K.; Tavshanov, I. On the possibility of implementing a simple shear in the cross-section of metal materials during caliber rolling. *Eng. Solid Mech.* **2023**, *11*, 253–262. [CrossRef]
31. Mashekov, S.; Nurtazaev, E.; Mashekova, A.; Abishkenov, M. Extruding aluminum bars on a new structure radial shear mill. *Metalurgija* **2021**, *60*, 427–430.
32. Arbuz, A.; Kawalek, A.; Ozhmegov, K.; Dyja, H.; Panin, E.; Lepsibayev, A.; Sultanbekov, S.; Shamenova, R. Using of Radial-Shear Rolling to Improve the Structure and Radiation Resistance of Zirconium-Based Alloys. *Materials* **2020**, *13*, 4306. [CrossRef]
33. Abishkenov, M.; Tavshanov, I.; Lutchenko, N.; Amanzholov, N.; Kalmyrzayev, D.; Ashkeyev, Z.; Nogaev, K.; Kydyrbayeva, S.; Abdirashit, A. Improving Mechanical Properties of Low-Quality Pure Aluminum by Minor Reinforcement with Fine B_4C Particles and T6 Heat Treatment. *Appl. Sci.* **2024**, *14*, 10773. [CrossRef]
34. Channar, H.R.; Ullah, B.; Naseem, M.S.; Akhter, J.; Mehmood, A.; Aamir, M. Mechanical Properties and Microstructural Investigation of AA2024-T6 Reinforced with Al_2O_3 and SiC Metal Matrix Composites. *Eng* **2024**, *5*, 3023–3032. [CrossRef]
35. Singhal, V.; Shelly, D.; Babbar, A.; Lee, S.-Y.; Park, S.-J. Review of Wear and Mechanical Characteristics of Al-Si Alloy Matrix Composites Reinforced with Natural Minerals. *Lubricants* **2024**, *12*, 350. [CrossRef]
36. Kareem, A.; Qudeiri, J.A.; Abdudeen, A.; Ahammed, T.; Ziout, A. A Review on AA 6061 Metal Matrix Composites Produced by Stir Casting. *Materials* **2021**, *14*, 175. [CrossRef] [PubMed]
37. Abishkenov, M.; Tavshanov, I.; Lutchenko, N.; Nogaev, K.; Kalmyrzayev, D.; Abdirashit, A.; Aikenbayeva, N. Effect of Minor Reinforcement with Ultrafine Industrial Microsilica Particles and T6 Heat Treatment on Mechanical Properties of Aluminum Matrix Composites. *Appl. Sci.* **2025**, *15*, 1329. [CrossRef]

38. Razzaq, A.M.; Majid, D.L.; Basheer, U.M.; Aljibori, H.S.S. Research Summary on the Processing, Mechanical and Tribological Properties of Aluminium Matrix Composites as Effected by Fly Ash Reinforcement. *Crystals* **2021**, *11*, 1212. [CrossRef]
39. Farooq, S.A.; Mukhtar, S.H.; Raina, A.; Ul Haq, M.I.; Siddiqui, M.I.H.; Naveed, N.; Dobrota, D. Effect of TiB_2 on the Mechanical and Tribological Properties of Marine Grade Aluminum Alloy 5052: An Experimental Investigation. *J. Mater. Res. Technol.* **2024**, *29*, 3749–3758. [CrossRef]
40. Rane, K.; Dhokey, N. On the Formation and Distribution of In Situ Synthesized TiB_2 Reinforcements in Cast Aluminium Matrix Composites. *J. Compos. Sci.* **2018**, *2*, 52. [CrossRef]
41. Bhowmik, A.; Sen, B.; Beemkumar, N.; Singh Chohan, J.; Bains, P.S.; Singh, G.; Kumar, A.V.; Santhosh, A.J. Development and wear resistivity performance of SiC and TiB_2; particles reinforced novel aluminium matrix composites. *Results Eng.* **2024**, *24*, 102981. [CrossRef]
42. Alfattani, R.; Yunus, M. Explorations of mechanical and corrosion resistance properties of AA6063/TiB_2/Cr_2O_3 hybrid composites produced by stir casting. *J. Sci. Adv. Mater. Devices* **2024**, *9*, 100790. [CrossRef]
43. ELDeeb, I.S.; Hawam, A.A.; Nabhan, A.; Egiza, M. Efficient formability in Radial-Shear Rolling of A2024 aluminum alloy with screw rollers. *Mater. Today Commun.* **2024**, *41*, 110241. [CrossRef]
44. *ASTM E8*; Standard Test Methods for Tension Testing of Metallic Materials. ASTM International: West Conshohocken, PA, USA, 2021. [CrossRef]
45. *ASTM E384-22*; Standard Test Method for Microindentation Hardness of Materials. ASTM International: West Conshohocken, PA, USA, 2022. [CrossRef]
46. Prasad, D.S.; Shoba, C.; Ramanaiah, N. Investigations on mechanical properties of aluminum hybrid composites. *J. Mater. Res. Technol.* **2014**, *3*, 79–85. [CrossRef]
47. *ASTM D792-20*; Standard Test Methods for Density and Specific Gravity (Relative Density) of Plastics by Displacement. ASTM International: West Conshohocken, PA, USA, 2020. [CrossRef]
48. Doddapaneni, S.; Kumar, S.; Sharma, S.; Shankar, G.; Shettar, M.; Kumar, N.; Aroor, G.; Ahmad, S.M. Advancements in EBSD Techniques: A Comprehensive Review on Characterization of Composites and Metals, Sample Preparation, and Operational Parameters. *J. Compos. Sci.* **2025**, *9*, 132. [CrossRef]
49. Carneiro, Í.; Fernandes, J.V.; Simões, S. Microstructural Characterization of Al/CNTs Nanocomposites after Cold Rolling. *Nanomaterials* **2023**, *13*, 1362. [CrossRef] [PubMed]
50. Carneiro, Í.; Fernandes, J.V.; Simões, S. Deformation Behaviour of Cold-Rolled Ni/CNT Nanocomposites. *Appl. Sci.* **2022**, *12*, 9471. [CrossRef]
51. Prabhu, D.; Rao, P. Corrosion behaviour of 6063 aluminium alloy in acidic and in alkaline media. *Arab. J. Chem.* **2017**, *10*, S2234–S2244. [CrossRef]
52. Samal, P.; Mandava, R.K.; Vundavilli, P.R. Dry sliding wear behavior of Al 6082 metal matrix composites reinforced with red mud particles. *SN Appl. Sci.* **2020**, *2*, 313. [CrossRef]
53. Vivekananda, A.S.; Prabu, S.B. Wear Behaviour of In Situ Al/TiB_2 Composite: Influence of the Microstructural Instability. *Tribol. Lett.* **2018**, *66*, 41. [CrossRef]
54. Dhokey, N.B.; Rane, K.K. Wear Behavior and Its Correlation with Mechanical Properties of TiB_2 Reinforced Aluminium-Based Composites. *Adv. Tribol.* **2011**, *9–10*, 837469. [CrossRef]
55. Balakrishnan, M.; Dinaharan, I.; Kalaiselvan, K.; Palanivel, R. Friction stir processing of Al_3Ni intermetallic particulate reinforced cast aluminum matrix composites: Microstructure and tensile properties. *J. Mater. Res. Technol.* **2020**, *9*, 4356–4367. [CrossRef]
56. Elkady, O.A.; Alouba, M.; Ali, A.I.; Choi, D.; Nouh, F. Non-destructive void analysis of Al6063–SiC nanocomposites for gamma shielding applications. *J. Mater. Sci. Mater. Electron.* **2025**, *36*, 1423. [CrossRef]
57. Jandaghi, M.R.; Pouraliakbar, H.; Khalaj, G.; Khalaj, M.-J.; Heidarzadeh, A. Study on the post-rolling direction of severely plastic deformed Aluminum-Manganese-Silicon alloy. *Arch. Civ. Mech. Eng.* **2016**, *16*, 876–887. [CrossRef]
58. Mamaghani, K.R.; Kazeminezhad, M. The Effect of Direct and Cross-Rolling on Mechanical Properties and Microstructure of Severely Deformed Aluminum. *J. Mater. Eng. Perform.* **2014**, *23*, 115–124. [CrossRef]
59. Poria, S.; Sahoo, P.; Sutradhar, G. Tribological Characterization of Stir-cast Aluminium-TiB_2 Metal Matrix Composites. *Silicon* **2016**, *8*, 591–599. [CrossRef]
60. Ayar, V.S.; Sutaria, M.P. Comparative Evaluation of Ex Situ and In Situ Method of Fabricating Aluminum/TiB_2 Composites. *Inter. Metalcast.* **2021**, *15*, 1047–1056. [CrossRef]
61. Vivekananda, A.S.; Balasivanandha Prabu, S.; Paskaramoorthy, R. Combined effect of process parameters during aluminothermic reaction process on the microstructure and mechanical properties of in situ Al/TiB_2 composite. *J. Alloys Compd.* **2018**, *735*, 619–634. [CrossRef]
62. Auradi, V.; Kori, S.A. Influence of reaction temperature for the manufacturing of Al–3Ti and Al–3B master alloys. *J. Alloys Compd.* **2008**, *453*, 147–156. [CrossRef]

63. Cui, Y.; King, D.J.M.; Horsfield, A.P.; Gourlay, C.M. Solidification orientation relationships between Al_3Ti and TiB_2. *Acta Mater.* **2020**, *186*, 149–161. [CrossRef]
64. Golla, C.B.; Babar Pasha, M.; Rao, R.N.; Ismail, S.; Gupta, M. Influence of TiC Particles on Mechanical and Tribological Characteristics of Advanced Aluminium Matrix Composites Fabricated through Ultrasonic-Assisted Stir Casting. *Crystals* **2023**, *13*, 1360. [CrossRef]
65. Madhukar, P.; Mishra, V.; Selvaraj, N.; Rao, C.S.P.; Gonal Basavaraja, V.K.; Seetharam, R.; Chavali, M.; Mohammad, F.; Soleiman, A.A. Influence of Ultrasonic Vibration towards the Microstructure Refinement and Particulate Distribution of AA7150-B_4C Nanocomposites. *Coatings* **2022**, *12*, 365. [CrossRef]
66. Balasubramani, N.; StJohn, D.; Dargusch, M.; Wang, G. Ultrasonic Processing for Structure Refinement: An Overview of Mechanisms and Application of the Interdependence Theory. *Materials* **2019**, *12*, 3187. [CrossRef] [PubMed]
67. Qiu, J.; Li, Y.; Luo, X.; Zhou, H.; Cao, C.; Bi, G. Silicon regulation of the interface microstructure and shear strength of rheological cast-rolling aluminum/steel composite plates. *J. Mater. Res. Technol.* **2024**, *30*, 6812–6828. [CrossRef]
68. Luo, K.-G.; Wu, Y.-Z.; Xiong, H.-Q.; Zhang, Y.; Kong, C.; Yu, H.-L. Enhanced mechanical properties of aluminum matrix composites reinforced with high-entropy alloy particles via asymmetric cryorolling. *Trans. Nonferrous Met. Soc. China* **2023**, *33*, 1988–2000. [CrossRef]
69. Wang, Z.J.; Zheng, Z.; Fu, M.W. Aluminum matrix composites: Structural design and microstructure evolution in the deformation process. *J. Mater. Res. Technol.* **2024**, *30*, 3724–3754. [CrossRef]
70. Geng, R.; Qiu, F.; Jiang, Q.-C. Reinforcement in Al Matrix Composites: A Review of Strengthening Behavior of Nano-Sized Particles. *Adv. Eng. Mater.* **2018**, *20*, 1701089. [CrossRef]
71. Schwarze, C.; Darvishi Kamachali, R.; Steinbach, I. Phase-field study of zener drag and pinning of cylindrical particles in polycrystalline materials. *Acta Mater.* **2016**, *106*, 59–65. [CrossRef]
72. Wang, X.; Guo, M.; Moliar, O.; Peng, W.; Xie, C.; Chen, J.; Wang, Y. Enhanced grain refinement and texture weakening in Al–Mg–Si alloy through a novel thermomechanical processing. *J. Alloys Compd.* **2022**, *925*, 166654. [CrossRef]
73. Peng, J.; Zhang, Z.; Liu, Z.; Li, Y.; Guo, P.; Zhou, W.; Wu, Y. The effect of texture and grain size on improving the mechanical properties of Mg-Al-Zn alloys by friction stir processing. *Sci. Rep.* **2018**, *8*, 4196. [CrossRef]
74. Wang, S.; Zhuang, Q.; Liu, W.; Liu, X.; Badreddine, H.; Saba, F.; Li, Z.; Yue, Z. Simulation and Discussion on Strength Mechanism of Trimodal Grain-Structured CNT/Al Composites Using Strain Gradient Theory. *J. Compos. Sci.* **2024**, *8*, 490. [CrossRef]
75. Mantha, S.R.V.; Kumar, G.B.V.; Pramod, R.; Rao, C.S.P. Investigations on Microstructure, Mechanical, and Wear Properties, with Strengthening Mechanisms of Al6061-CuO Composites. *J. Manuf. Mater. Process.* **2024**, *8*, 245. [CrossRef]
76. Wang, C.; Zhu, X.; Zhang, K.; Liu, J.; Xiao, X.; Jiang, C.; Zhang, J.; Lv, C.; Sun, Z. Microstructures and Mechanical Properties of Al Matrix Composites Reinforced with TiO_2 and Graphitic Carbon Nitride. *Metals* **2025**, *15*, 60. [CrossRef]
77. Kumar, A.; Rana, R.S.; Purohit, R.; Saxena, K.K.; Xu, J.; Malik, V. Metallographic Study and Sliding Wear Optimization of Nano Si_3N_4 Reinforced High-Strength Al Metal Matrix Composites. *Lubricants* **2022**, *10*, 202. [CrossRef]